

www.acsami.org Research Article

# In Situ Formation of 3D Cross-Linked Binders in Silicon—Graphite Composite Anodes for All-Solid-State Lithium Batteries

Young-Jun Lee, Won-Jae Song, Yong-Han Jo, Han-Jo Lee, Yunsung Kim, Gahyeon Im, and Dong-Won Kim\*



Cite This: ACS Appl. Mater. Interfaces 2025, 17, 57114-57123



**ACCESS** I Metrics & More Article Recommendations Supporting Information ົ້ວ 1200 @ 0.3 C and 30 °C (mgh 1000 Discharge capacity 800 600 400 Sulfide solid electrolyte 200 Cross-linked binder 50 100 150 200

ABSTRACT: All-solid-state lithium batteries (ASSLBs) with sulfide-based solid electrolytes offer improved safety compared to conventional lithium-ion batteries. Silicon-based anode materials enable an increase in the energy density of ASSLBs. However, the substantial volume change during cycling induces interfacial degradation, leading to significant capacity loss. In this study, the composite silicon–graphite (Si–C) anodes were fabricated via an in situ cross-linking reaction between polybutadiene (PBD) and n-butyl acrylate monomer. The resulting three-dimensional cross-linked polymer binder significantly improved interfacial adhesion and cycling stability of the composite anode. Furthermore, the influence of PBD isomeric structure on cross-linking selectivity was investigated to optimize the electrochemical performance and mechanical properties of the composite anode. As a result, the composite anode employing solid electrolyte ( $\text{Li}_6\text{PS}_5\text{Cl}_{0.5}\text{Br}_{0.5}$ ) and highly cross-linked binder based on cis-PBD delivered a high initial discharge capacity of 1056.3 mAh g<sup>-1</sup> (areal capacity: 3.8 mAh cm<sup>-2</sup>) and exhibited superior capacity retention at 0.3 C and 30 °C.

Cycle number

KEYWORDS: silicon—graphite composite anode, cross-linked binder, sulfide solid electrolyte, all-solid-state lithium battery, in situ cross-linking

## ■ INTRODUCTION

As the demand for electric vehicles continues to grow in efforts to reduce carbon emissions, the development of rechargeable batteries with enhanced safety and higher energy density has become increasingly critical. 1/2 In this context, all-solid-state lithium batteries (ASSLBs) using solid electrolytes have attracted considerable attention as next-generation energy storage systems.<sup>3-9</sup> In particular, ASSLBs incorporating sulfide-based solid electrolytes, such as Li<sub>10</sub>GeP<sub>2</sub>S<sub>12</sub>, Li<sub>2</sub>S- $P_2S_5$ , Li<sub>6</sub>PS<sub>5</sub>X (X = Cl, Br, I), have garnered significant interest due to their high ionic conductivity and superior processability compared to oxide-based solid electrolytes. 10-13 To achieve higher energy density in ASSLBs, the use of anode active materials with high specific capacity is a promising approach. Silicon (Si), in particular, offers a remarkably high theoretical specific capacity (~4200 mAh g<sup>-1</sup>). Moreover, silicon has additional advantages, including natural abundance, low cost, and the absence of lithium dendrite formation in contrast to lithium metal anodes. 14-17 Despite these benefits, its substantial volume changes during repeated cycling result in the cracking and pulverization of silicon particles, as well as the formation of numerous voids in the composite anode, which significantly limit the practical application of pure silicon as an active material. To address these challenges, silicongraphite (Si–C) composites have been proposed as a viable alternative, owing to the high electronic conductivity of graphite and its ability to buffer the volume changes of silicon. Nevertheless, interfacial contact issues in the composite Si–C anode still remain unresolved, primarily due to the persistent volume changes of silicon during cycling. The use of highly adhesive and mechanically robust polymer

Received: July 26, 2025
Revised: September 23, 2025
Accepted: September 23, 2025
Published: October 6, 2025





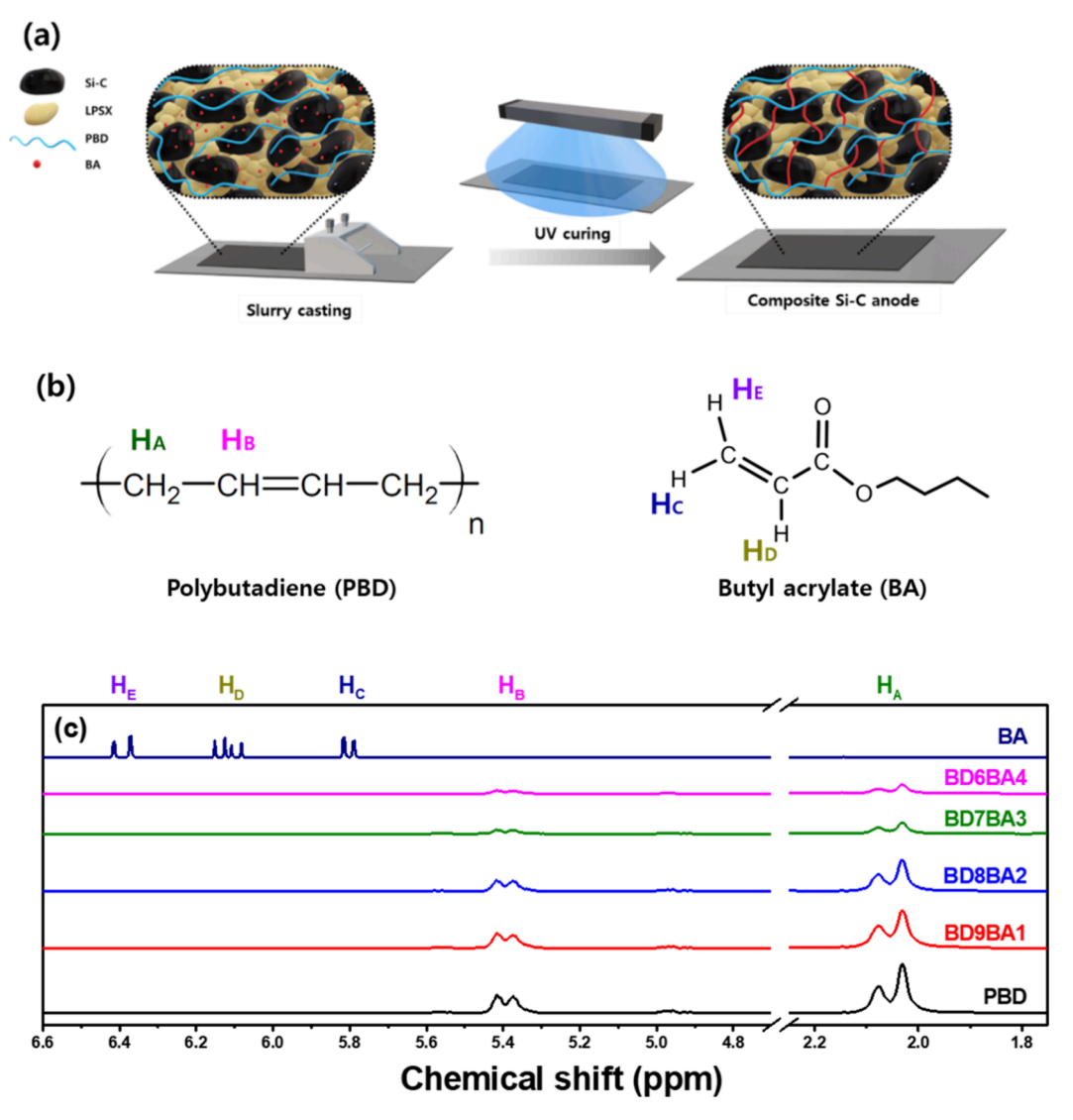


Figure 1. (a) Schematic illustration of the preparation process for the composite Si–C anode using an in situ cross-linked binder. (b) Chemical structures of polybutadiene and *n*-butyl acrylate. (c) <sup>1</sup>H NMR spectra of PBD, BA, and the cross-linked binders (BDxBAy).

binders can enhance the interfacial properties of Si-based composite anodes by improving the contact between the electrode components. <sup>24–27</sup> In this regard, extensive research has been devoted to identifying suitable polymer binders for use in composite anodes for ASSLBs. The wet-slurry method that use organic solvents to fabricate composite electrodes offers advantages in terms of mass productivity. However, selecting an appropriate polymer binder for this process remains challenging due to the poor chemical compatibility between sulfide-based solid electrolytes and commonly used organic solvents. Although polymer binders containing highly polar functional groups can effectively improve interfacial contact within the composite electrode, they tend to dissolve only in polar solvents that can disrupt the crystal structure of sulfide-based solid electrolytes. <sup>28–31</sup> Consequently, the limited binder selection impairs the interfacial integrity of the composite electrode. More importantly, these constraints hinder the mitigation of silicon's volume expansion, leading to the formation of voids and cracks within the composite anode.

In this work, we propose the use of a highly adhesive and robust cross-linked binder to mitigate the volume changes of the composite Si-C anode for ASSLBs. Polybutadiene (PBD) and *n*-butyl acrylate (BA) monomer were utilized to induce an in situ chemical cross-linking reaction between them within the composite Si-C anode. This cross-linking reaction formed three-dimensional polymer networks, which enhanced the mechanical integrity of the composite anode and improved interfacial contacts among the electrode components.<sup>32</sup> Thus, the composite Si-C anode employing the in situ cross-linked binder exhibited improved cycling stability and high-rate performance compared to that using non-cross-linked PBD. Furthermore, the effect of PBD isomer structure on the selectivity of the cross-linking reaction was investigated to further enhance the electrochemical and mechanical properties of the anode. As a result, the anode employing Si-C, solid electrolyte (Li<sub>6</sub>PS<sub>5</sub>Cl<sub>0.5</sub>Br<sub>0.5</sub>, LPSX), and highly cross-linked binder based on cis-PBD delivered a high initial discharge capacity of 1056.3mAhg-1 and exhibited good capacity retention at 0.3 C and 30 °C. In addition, field-emission scanning electron microscopy (FE-SEM) and high-resolution 3D X-ray microscopy (XRM) analyses revealed minimal thickness change and less void formation in the anode with cross-linked binder exhibited after cycling.

### EXPERIMENTAL SECTION

Materials. The argyrodite-type solid electrolyte Li<sub>6</sub>PS<sub>5</sub>Cl<sub>0.5</sub>Br<sub>0.5</sub> (LPSX) was synthesized via mechanochemical milling. A stoichiometric mixture of Li<sub>2</sub>S (99.9%, Alfa Aesar), P<sub>2</sub>S<sub>5</sub> (99%, Sigma-Aldrich), LiCl (99.9%, Alfa Aesar), and LiBr (99%, Sigma-Aldrich) was ball-milled with zirconia balls at 500 rpm for 12 h in a zirconia vial using a Pulverisette 7PL (Fritsch GmbH). The milled powder was then subjected to heat treatment at 550 °C for 6 h. The Si-graphite composite was synthesized using ball-milled graphite flakes (Fritsch), Si powder (Hanbyul), and sucrose (Sigma-Aldrich), as previously reported.<sup>33,34</sup> In brief, graphite flakes, Si, and sucrose were homogeneously dispersed in deionized water, followed by spray drying with a spray dryer (Eyela) at 500 rpm and 110 °C. Polybutadiene (PBD, Sigma-Aldrich) and cis-polybutadiene (cis-PBD, Sigma-Aldrich) were dried overnight in vacuum oven prior to use. N-butyl acrylate (BA, ≥99%, Sigma-Aldrich) was used after removing inhibitor by passing it through basic alumina columns, followed by drying over molecular sieves. N-butyl butyrate (Alfa Aesar) was also dried using molecular sieves prior to use. 2-Hydroxy-2-methylpropiophenone (HMPP, 97%, Sigma-Aldrich) was used as the photoinitiator. Lithium foil with a thickness of 200  $\mu$ m was purchased from Honjo Metal.

Fabrication of Composite Si–C Electrodes. The composite Si–C anode was fabricated using a wet-slurry casting method. The polymer (PBD or cis-PBD) was first dissolved in n-butyl butyrate, followed by the addition of an appropriate amount of BA monomer and HMPP (5 wt % relative to BA) to prepare the binder solution. Slurries were then prepared by homogeneously mixing Si–C, LPSX, and the binder in a weight ratio of 70:30:2 using a planetary mixer (Thinky Mixer, AR-100). The resulting slurry was cast onto a Ni foil using a doctor blade and subsequently exposed to UV irradiation ( $\lambda$  = 254 nm) for 15 min. For comparison, composite Si–C anodes employing PBD or a simply mixed binder (BD7BA3-mix) were also prepared by casting slurries of Si–C, LPSX, and binder onto Ni foil. All the composite anodes were dried in a vacuum oven at 70 °C for 12 h to remove residual solvents. Si–C was incorporated into the composite anodes at a mass loading of 3.6 mg cm<sup>-2</sup>.

Characterization. <sup>1</sup>H and <sup>13</sup>C nuclear magnetic resonance (NMR) spectroscopy were performed using a VNMRS 600 MHz spectrometer (Varian) to investigate residual monomers and the chemical structure of the cross-linked binder. X-ray diffraction (XRD) measurements were conducted using a high-resolution diffractometer (D8 ADVANCE, Bruker) with Cu K $\alpha$  radiation ( $\lambda = 1.5418$  Å) to examine changes in the crystalline structure of LPSX and Si-C. The reactivity of PBD isomers with BA was investigated by Raman spectroscopy using a DXR-3xi Raman Imaging Microscope. The cohesive strength of the composite anode was evaluated using a surface and interfacial cutting analysis system (SAICAS, Daipla Wintes) equipped with a 1 mm-wide diamond blade. The change in the anode thickness after cycling was examined using field-emission scanning electron microscopy (FE-SEM, Verios G4 UC). The crosssectional morphologies of the composite electrodes were investigated using FE-SEM and energy-dispersive spectroscopy (EDS). Internal voids within the composite anode after cycling were analyzed using high-resolution 3D X-ray microscopy (XRM) combined with computed tomography (Xradia 620 Versa, Carl Zeiss). The acquired raw data were processed using Dragonfly imaging software (Object Research Systems, ORS) to reconstruct the 3D structure of the composite anode and to quantify its porosity.

**Electrochemical Measurement.** The all-solid-state cell was fabricated in the following sequence. First, a solid electrolyte pellet was prepared by cold-pressing 150 mg of LPSX into a ~600 μm-thick pellet under a pressure of 105 MPa. Next, the anode was put on top of the solid electrolyte and pressed at 430 MPa. Finally, lithium metal was put on the opposite side of the pellet, and the entire cell was pressed under a pressure of 60 MPa. All cell assembly procedures were conducted in an Ar-filled glovebox (MBRAUN). Cycling performance was evaluated using a battery cycler (TOSCAT-3100, Toyo). Prior to the cycling tests, three preconditioning cycles were

conducted at 0.1 C (1 C = 4.0 mA cm $^{-2}$ ). The cell was then cycled at 0.3 C rate within a voltage range of 0.01–1.5 V. For rate capability testing, charge—discharge tests were conducted at current rates ranging from 0.1 to 1.0 C. The DC internal resistance (DC-IR) of the cell was calculated based on the linear slope of the I–V curve. To measure DC-IR, the cell was initially cycled at 0.1 C and charged up to 0.15 V, followed by a 10 min rest. Subsequently, a series of charge—discharge pulses at increasing C-rates (from 0.025 to 1.0 C) were applied for 10 s each, with a 20 min rest period between pulses. All the electrochemical tests were carried out at 30  $^{\circ}$ C.

### ■ RESULTS AND DISCUSSION

Wet slurry casting was employed to fabricate the composite Si-C anode using in situ cross-linked binder. As illustrated in Figure 1a, a homogeneously mixed slurry containing Si-C, LPSX, and binder solution was cast onto a Ni current collector, followed by UV irradiation for 15 min. Free radicals generated by the photoinitiator (2-hydroxy-2-methylpropiophenone, HMPP) activate the double bonds of both PBD and BA, initiating radical polymerization by forming linkages with nearby monomers and polymers. The cross-linked binder was prepared with varying ratios of PBD and BA to determine their optimal composition. In this work, the cross-linked binder is denoted by the molar ratio of C=C double bonds in PBD and BA. For example, the cross-linked binder with PBD and BA in the molar ratio of x:y was designated as BDxBAy. The chemical structure of the cross-linked binders was analyzed using <sup>1</sup>H NMR spectroscopy. The <sup>1</sup>H NMR spectra of PBD, BA monomer, and the cross-linked polymers (BDxBAy) are presented in Figure 1c. The broad peaks at 1.96-2.14 ppm and 5.30-5.45 ppm correspond to the -CH<sub>2</sub>- and -CH= protons, respectively, and are labeled as H<sub>A</sub> and H<sub>B</sub> (Figure 1b). The peaks observed around 5.79–6.37 ppm are attributed to the protons of the C=C double bond in BA and are designated as H<sub>C</sub>, H<sub>D</sub>, and H<sub>E</sub> (Figure 1b). In the <sup>1</sup>H NMR spectra, the three proton peaks (H<sub>C</sub>, H<sub>D</sub>, and H<sub>E</sub>) completely disappeared after the cross-linking reaction between PBD and BA, and the intensity ratio of H<sub>B</sub> to H<sub>A</sub> gradually decreased with increasing BA content, as summarized in Table S1. These results suggest that unreacted BA monomers are absent in the cross-linked polymers, and some of the C=C double bonds in PBD participated in the cross-linking reaction with BA monomer. Figure S1 presents the <sup>1</sup>H NMR spectra of the cross-linked polymers and poly(butyl acrylate) (PBA) homopolymer. As shown in figure, the H<sub>C</sub>, H<sub>D</sub>, and H<sub>E</sub> peaks corresponding to the BA monomer cannot be observed in PBA, and the -CH2- proton peaks adjacent to the ester group (-COO-), labeled as H<sub>F</sub>, upfield shift and change from three split peaks to broad peaks upon polymerization.<sup>35</sup> Furthermore, the H<sub>E</sub> peaks in the cross-linked polymers exhibit a downfield shift (deshielding) with increasing PBD content. This result indicates that electron delocalization is induced by the C=C double bonds of PBD in the cross-linked polymer. 36-3

The main obstacle in wet slurry casting for fabricating composite electrodes is the structural collapse of the sulfide solid electrolyte (LPSX) caused by the polar solvents used to dissolve the polymer binder. To investigate the chemical compatibility of LPSX with solvent or polymer binders, X-ray diffraction (XRD) analysis was performed to examine changes in the crystalline structure of LPSX during the electrode fabrication process. Figure S2 presents the XRD patterns of LPSX, Si–C, and composite Si–C anodes using either PBD binder or cross-linked binders (BDxBAy). The XRD results

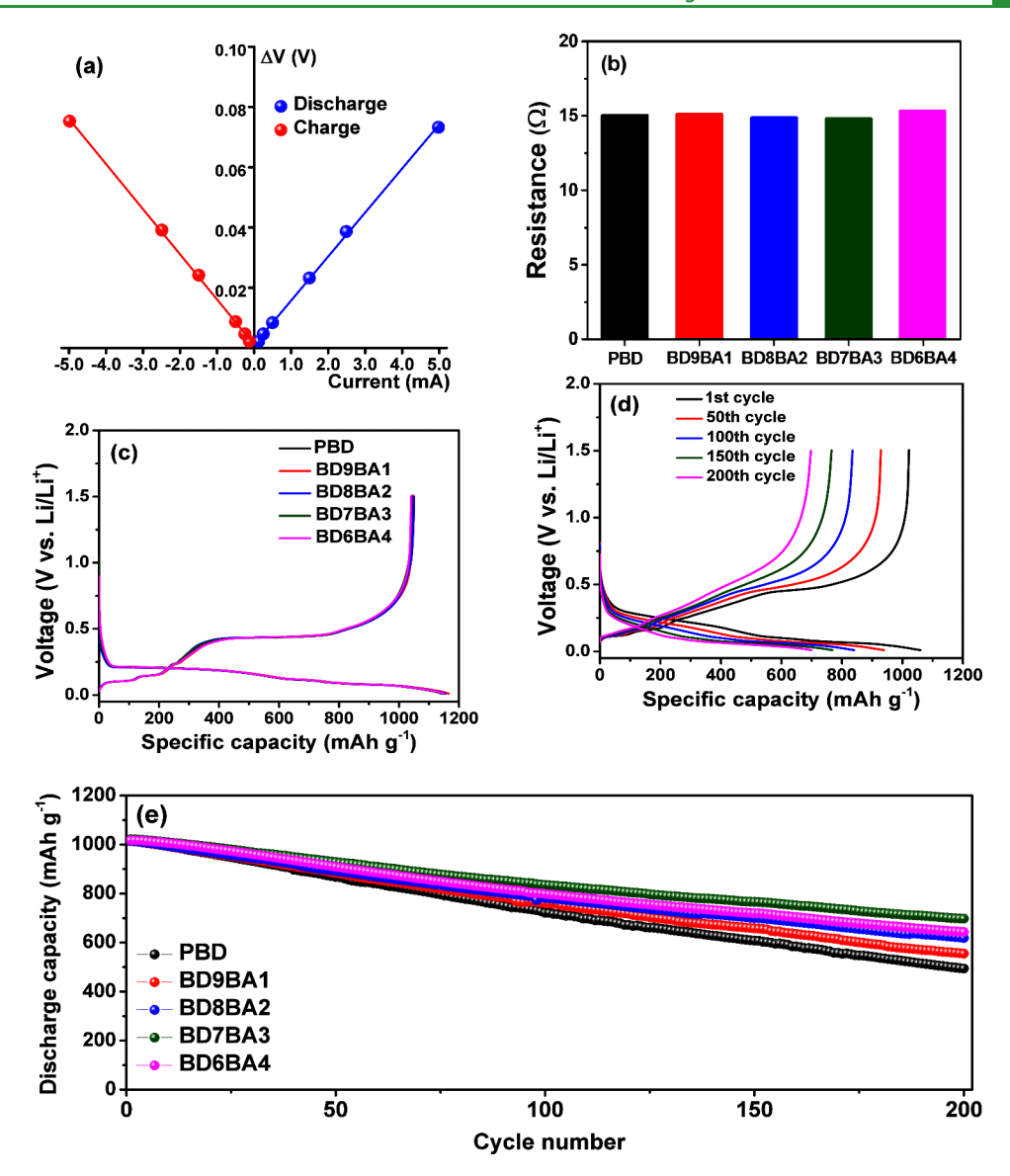


Figure 2. (a) Plots of voltage change versus current for the Li/LPSX/Si–C cell with BD7BA3. (b) Resistances of Li/LPSX/Si–C cells employing different binders. (c) Voltage curves of the Li/LPSX/Si–C cells during the first preconditioning cycle at 0.1 C and 30 °C. (d) Cycling curves of the Li/LPSX/Si–C cell with BD7BA3 at 0.3 C and 30 °C. (e) Cycling performance of the Li/LPSX/Si–C cells employing different binders at 0.3 C and 30 °C.

indicate that all the characteristic crystalline peaks of Si-C and LPSX in the composite anodes remained unchanged, suggesting that no side reactions occurred during the wet electrode fabrication process. Moreover, we performed linear sweep voltammetry on the solid electrolyte sheet incorporating the cross-linked binder within the potential range of 1.5-0.01 V (vs Li/Li<sup>+</sup>) (Figure S3). Although some reductive current was observed in this range, attributable to the inherent instability of the sulfide-based solid electrolyte, the solid electrolyte sheets with cross-linked binders exhibited no additional peaks compared to the pristine solid electrolyte. These results confirm that the cross-linked binder is electrochemically stable within the operational voltage window. The internal resistance of the anodes with various binders was determined by linear regression analysis of voltage increment  $(\Delta V)$  versus current (I) plots at various current densities in Figure S4.<sup>39</sup> The resistance was calculated from the slope of the I  $-\Delta V$  plot (Figure 2a), and the results are depicted in Figure 2b. As shown in the figure, the anodes exhibited

negligible differences in internal resistance regardless of the type of polymer binder, indicating that there was no significant increase in internal resistance due to the in situ cross-linking of PBD and BA. The cycling performance of the Si-C anode employing cross-linked binders with varying compositions was evaluated to determine the optimal ratio of PBD to BA. The counter electrode and solid electrolyte used to evaluate the electrochemical performance of the anode were lithium metal and LPSX, respectively (i.e., Li/LPSX/Si-C cell). The composite anode was labeled according to the polymer binder used in its preparation. During the first preconditioning cycle at 0.1 C and 30 °C, the anode delivered discharge capacities ranging from 1040.6 to 1050.7 mAh g<sup>-1</sup>, as shown in Figure 2c. Figures 2d and S5 show the voltage profiles of anodes with different binders at 0.3 C, while their cycling performance is compared in Figure 2e. Clearly, the anode prepared with crosslinked binders exhibited better cycling stability than the one using the PBD binder. The cross-linked network formed by PBD and BA helps mitigate the volume changes of Si-C in the

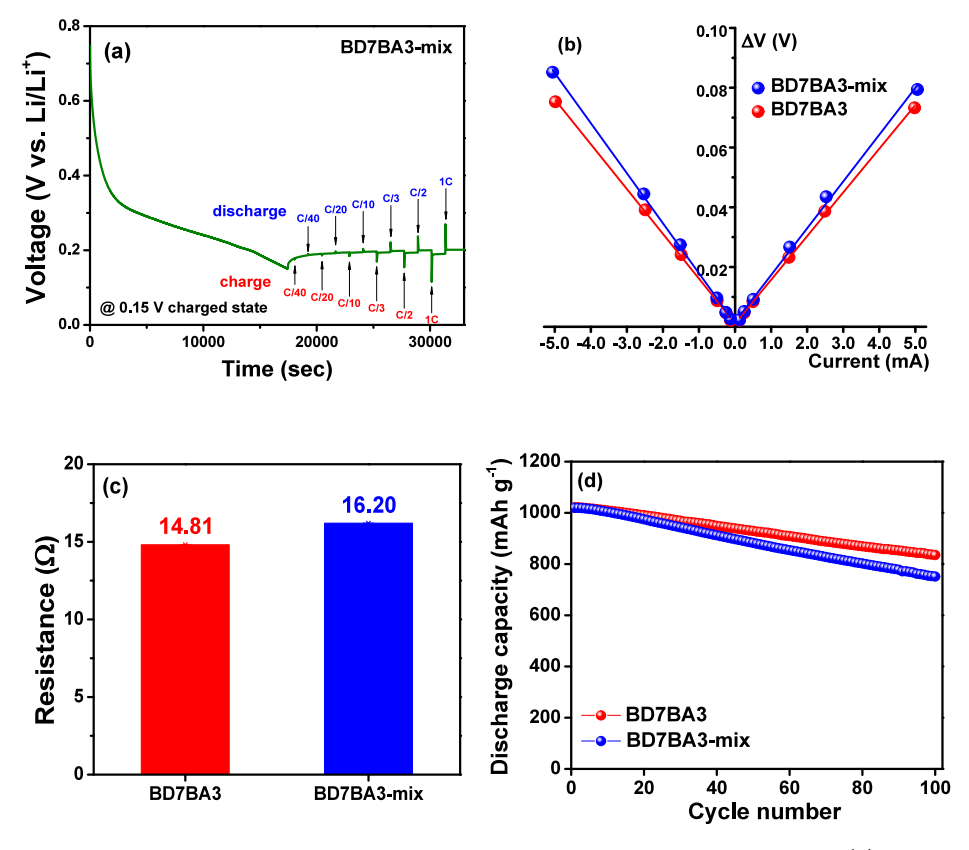


Figure 3. (a) Voltage response of the Li/LPSX/Si-C cell with BD7BA3-mix during the DC-IR experiment, (b) plot of voltage change versus current, and (c) resistances of the Li/LPSX/Si-C cells employing BD7BA3 and BD7BA3-mix binders. (d) Cycling performance of the Li/LPSX/Si-C cells using BD7BA3 and BD7BA3-mix binders at 0.3 C and 30 °C.

composite electrode, thereby maintaining good interfacial contacts between Si–C and LPSX and enhancing cycling stability. Among the cross-linked binders studied, BD7BA3 demonstrated the highest capacity retention, suggesting that the PBD to BA ratio of 7:3 is optimal for achieving superior cycling performance.

To investigate the effect of chemical cross-linking between PBD and BA, the composite Si-C anode was also prepared by simply mixing PBD and BA in the same weight ratio as BD7BA3, referred to as BD7BA3-mix. Figure S6 presents the <sup>1</sup>H and <sup>13</sup>C NMR spectra of PBD, PBA, BD7BA3, and BD7BA3-mix. In the <sup>1</sup>H NMR spectra, the H<sub>E</sub> peaks of BD7BA3 exhibited a downfield shift due to electron delocalization induced by the C=C double bonds in PBD, as previously discussed. In contrast, the H<sub>E</sub> peaks of BD7BA3mix did not show any noticeable changes in chemical shift. The carbon adjacent to the ester group (C<sub>A</sub>) appeared at 64.4 ppm in the <sup>13</sup>C NMR spectrum. The heteronuclear single-quantum correlation (HSQC) spectra in Figure S7 reveal that the methylene peaks of BD7BA3 (H<sub>E</sub> and C<sub>A</sub>) are downfield shifted. These results indicate that the in situ cross-linking reaction between PBD and BA results in the formation of a 3D polymer network. The distribution of the polymer binder within the composite Si-C electrodes, depending on the binder preparation method, was investigated by EDS mapping. Figure S8 shows the cross-sectional SEM and corresponding elemental mapping images of the Si-C anodes. The results reveal that Si from the active material, S from the solid electrolyte, and O from the polymer binder are homogeneously distributed, indicating that all components (Si-C, LPSX, and

binder) are uniformly dispersed throughout the composite without aggregation.

The internal resistance and electrochemical performance of the anodes prepared with BD7BA3 and BD7BA3-mix were compared. As shown in Figure 3, the use of the simply mixed binder (BD7BA3-mix) led to deteriorated electrochemical performance, as evidenced by increased internal resistance and reduced cycling stability. These results clearly indicate that the superior electrochemical properties of the anode using BD7BA3 originate from the cross-linked network structure formed by the binder, which effectively maintains strong binding among the electrode components within the composite anode.

To improve the cross-linking density of the 3D polymer network, we investigated which isomeric configuration of PBD predominantly undergoes radical cross-linking reactions. It is well-known that PBD consists of three different configurations — 1,4-cis, 1,4-trans, and 1,2-vinyl — which arise due to variations in synthesis conditions. He Raman spectra of PBD and BD7BA3 are shown in Figure 4a,b. The relative areas corresponding to the three configurations were calculated and are presented in Figure 4c. Notably, the peak associated with the 1,4-cis configuration decreased more significantly than those of the other configurations after cross-linking (30.4%  $\rightarrow$  25.7%), suggesting that 1,4-cis PBD primarily participates in the cross-linking reaction, thereby enhancing the cross-linking density of the polymer network.  $^{42,43}$ 

Accordingly, to further enhance the cross-linking density of the BD7BA3 binder, the Si—C anode was fabricated using cis-PBD and BA in the same weight ratio as BD7BA3. The cis-PBD consists of 99.0% 1,4-cis, 0.1% 1,4-trans, and 0.9% 1,2-

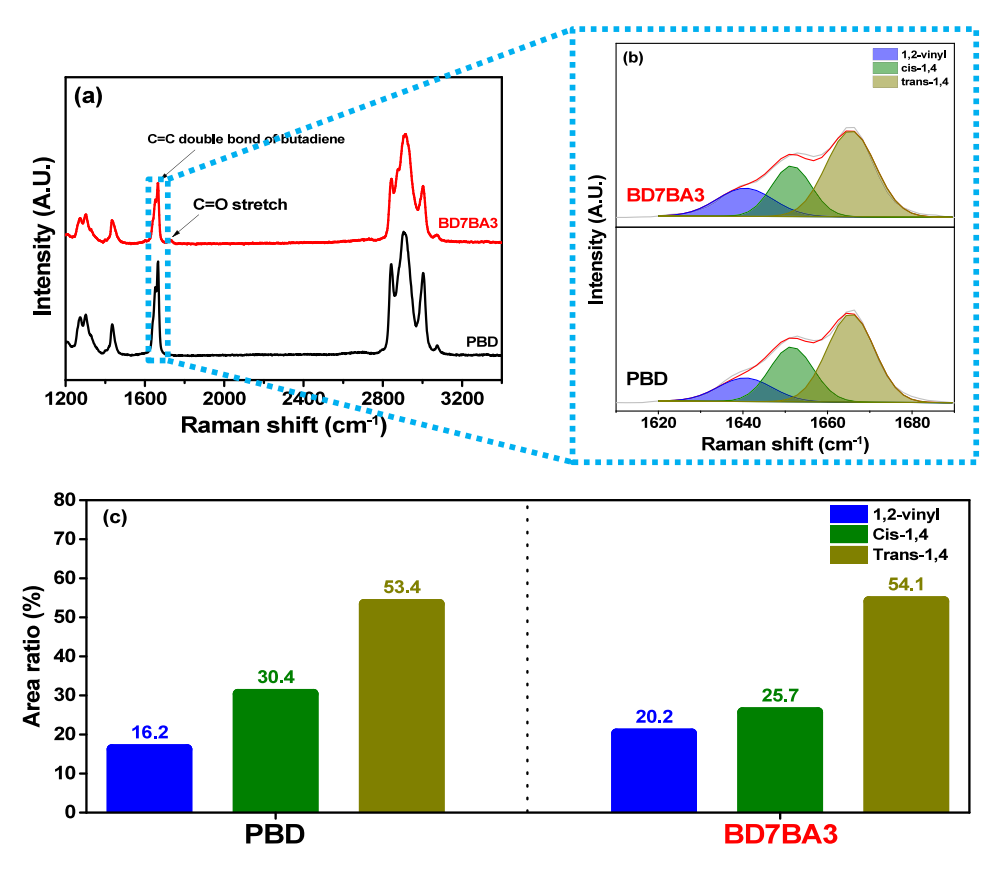


Figure 4. (a), (b) Raman spectra of PBD and BD7BA3. (c) Relative ratios of butadiene isomers in PBD and BD7BA3, as determined from the Raman spectra.

vinyl configurations. The resulting binder synthesized from cis-PBD and BA is referred to as cis-BD7BA3. To evaluate the cohesive properties of the composite anodes employing different binders (PBD, BD7BA3, and cis-BD7BA3), SAICAS measurements were performed.44 The horizontal and vertical forces required to cut through the middle of the composite anodes were measured using the constant velocity mode, as illustrated in Figure 5a. As shown in Figure 5b,c, the composite anodes prepared with cross-linked binders exhibited higher cutting forces, indicating that the 3D polymer network structure of the binder imparts enhanced cohesive strength among the components within the Si-C anode. Notably, the anode employing cis-BD7BA3 exhibited the highest horizontal and vertical forces, which can be ascribed to its highly crosslinked 3D polymer network structure. Moreover, nanoscratch tests were conducted to further evaluate the mechanical properties of the anodes.<sup>26</sup> Figure 5d shows a schematic illustration of the nanoscratch test. As depicted in Figure 5e, the anode fabricated with cis-BD7BA3 exhibited the smallest penetration depth, attributed to its superior mechanical properties. In addition, the DC-IR of the anodes with various binders was measured. As shown in Figure S9, the cell employing cis-BD7BA3 exhibited the lowest internal resistance. The lowest resistance in the DC-IR measurements is attributed to the strongest interfacial contact of the cis-PBDbased cross-linked binder, which enhances ionic pathways and reduces interfacial resistance. These results indicate that a wellconstructed 3D polymer network structure not only enhances the mechanical properties but also reduces the internal resistance of the composite anode.

The electrochemical performance of the anodes with different binders was evaluated. Figure 6a presents the representative cycling curves of the cell employing the cis-BD7BA3 binder, and Figure 6b illustrates a comparison of cycling performance among cells with different binders. It can be observed that the cis-BD7BA3 cell exhibited the best electrochemical performance in terms of both initial discharge capacity and cycling stability. It delivered a high initial discharge capacity of 1056.3 mAh g<sup>-1</sup> and retained 78.4% of its initial capacity after 200 cycles at 0.3 C and 30 °C. In comparison, the PBD and BD7BA3 cells showed capacity retentions of 48.7 and 68.3% at 200th cycle, respectively. Figures 6c and S10 show the cycling curves of the Li/LPSX/ Si-C cells with different binders at various C-rates, and their rate capabilities are compared in Figure 6d. The cis-BD7BA3 cell exhibited the lowest polarization at high current rates and consequently delivered the highest discharge capacities across all C-rates. The pressure variation of the cell during cycling was measured to investigate the effect of the polymer binder on mitigating the volume changes associated with the active Si-C materials. As shown in Figure S11, the cell employing cis-BD7BA3 exhibited the smallest pressure variations. This result indicates that the well-constructed 3D polymer network of cis-BD7BA3 effectively alleviates the volume changes in the Si-C electrode, thereby reducing the formation of cracks and voids within the Si-C anode. 45 To verify the operation of the cell under lower pressure, cells assembled with different binders were tested at a stack pressure of 15 MPa. As shown in Figure S12a, all cells exhibited lower discharge capacities and poorer cycling stability at 0.3 C compared with those operated under higher stack pressure. This result is likely due to lose particle

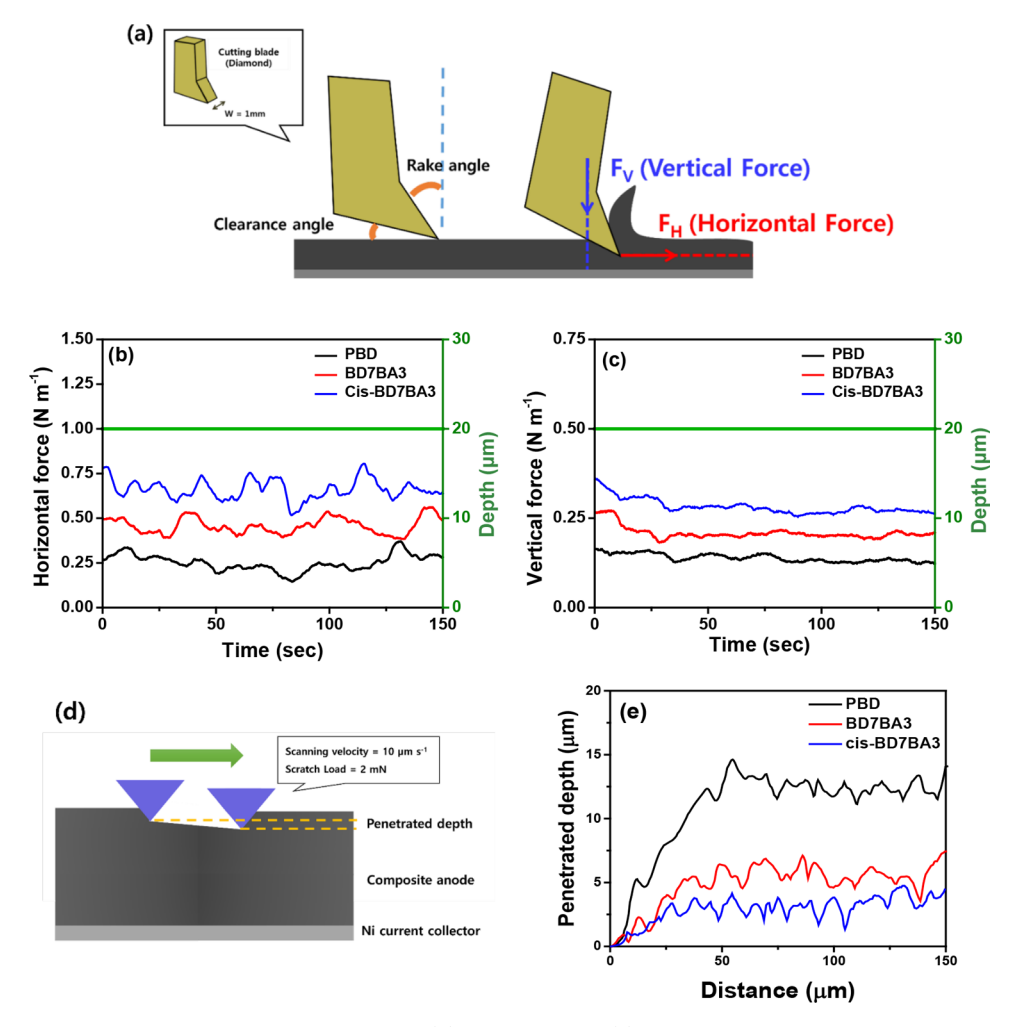


Figure 5. (a) Schematic illustrations of the SAICAS experiment. (b) Horizontal and (c) vertical forces required to cut and peel the composite Si–C anodes employing different binders. (d) Experimental scheme for nano scratch test and (e) penetration depth as a function of distance for composite Si–C anodes with various binders.

contacts, which increase internal resistance and deteriorate cell performance. Even under lower stack pressure, however, the cell employing cis-BD7BA3 exhibited the highest discharge capacity and the most stable cycling performance. These results can be attributed to the superior interfacial contact between the Si-C and LPSX, enabled by the highly adhesive and robust nature of the 3D polymer network binder, as previously discussed. In many previous studies, constant current/constant voltage (CC/CV) charging protocols have been applied during the lithiation process. In the CC/CV mode, the subsequent CV step transfers the residual charge into the electrode and enhances the overall capacity after CC charging. We evaluated the cycling performance of Li/Si-C cells under CC/CV conditions. As shown in Figure S12b, the CC/CV mode increased the discharge capacity of the cells by enabling residual charge storage after the CC step. Even under these testing conditions, the cell employing cis-BD7BA3 exhibited the best cycling performance owing to the superior binding properties of cis-BD7BA3.

Cross-sectional SEM images of the anodes were obtained in the discharged state, both before and after 200 cycles. Prior to cycling, the thickness of the composite anodes was approximately the same (~41  $\mu$ m), and all the electrodes exhibited intimate contact with the current collector, as shown in Figure 7a–c. However, as evident in Figure 7d,e, its

thickness significantly increased due to the large volume changes of the Si-C during repeated charge/discharge cycles. Notably, the composite Si-C anodes with cross-linked binders exhibited much smaller increases in their thickness. In particular, the composite anode prepared with cis-BD7BA3 showed the smallest thickness change, which is attributed to its strong cohesive properties enabled by the 3D polymer network structure. 46,47 The effect of binders on interfacial contacts after cycling was investigated using a 3D imaging analysis. X-ray microscopy (XRM), combined with microcomputed tomography ( $\mu$ -CT), was employed to evaluate the extent of internal void formation within the anode. 48,49 Specifically, the 3D morphology of the anode's internal structure was visualized. By capturing a series of 2D transmission images of the rotating sample, as shown in Figure S13, high-resolution 3D reconstructions of the composite Si-C electrodes were obtained through X-ray CT imaging. Figure 7g-i present the 3D morphologies of the composite anodes after 200 cycles, where internal pores are highlighted in red. After cycling, the porosities of the composite Si-C anodes prepared with PBD, BD7BA3, and cis-BD7BA3 were found to be 13.7, 7.3, and 6.0%, respectively. Furthermore, the composite anode with cis-BD7BA3 exhibited the lowest void count per unit volume, as shown in Figure S14. Cross-sectional SEM images and porosity analyses of the composite Si-C anodes were carried out in the

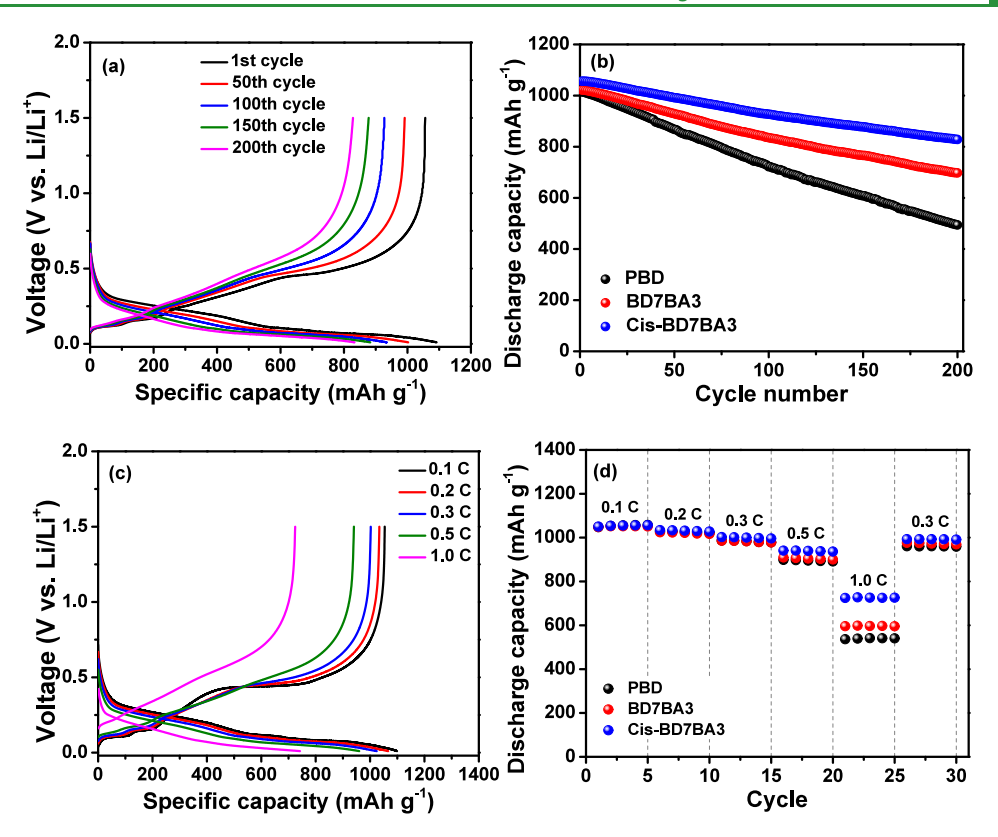


Figure 6. (a) Cycling curves of the Li/LPSX/Si-C cell with cis-BD7BA3 at 0.3 C and 30 °C. (b) Cycling performance of the Li/LPSX/Si-C cells employing different binders at 0.3 C and 30 °C. (c) Charge and discharge curves of the Li/LPSX/Si-C cell with cis-BD7BA3 at various current rates at 30 °C. (d) Comparison of discharge capacities of Li/LPSX/Si-C cells with different binders under various current rates at 30 °C.

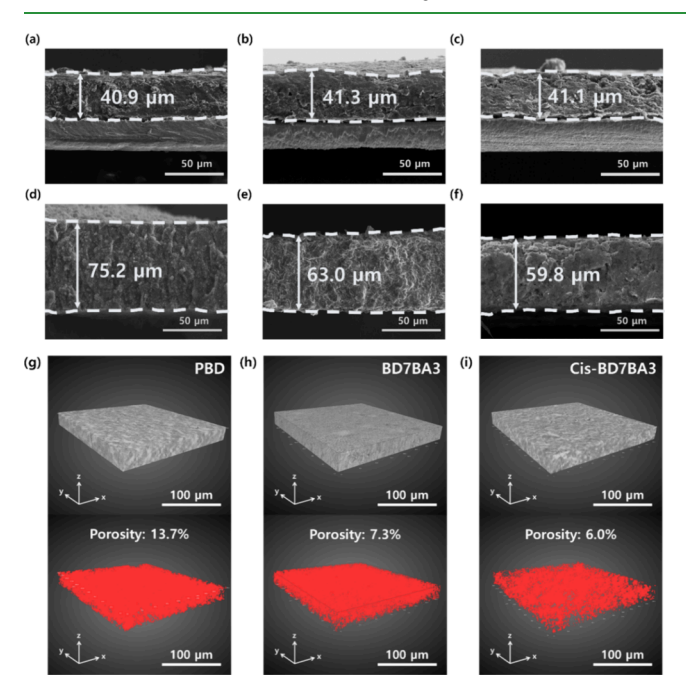


Figure 7. Comparison of cross-sectional SEM morphologies of Si-C composite anodes with different binders: images taken (a-c) before and (d-f) after 200 cycles. (a, d) PBD; (b, e) BD7BA3; and (c, f) cis-BD7BA3. X-ray microscopy (XRM) with microcomputed tomography ( $\mu$ -CT) of the composite Si-C anodes after 200 cycles. (g) PBD, (h) BD7BA3, and (i) cis-BD7BA3.

absence of external pressure, since direct examination under high stack pressure is challenging. If high stack pressure is

applied, the anodes would show significantly reduced thickness and porosity compared to the pressure-free condition. Nevertheless, it is evident that the highly cohesive cis-BD7BA3 enhances the interfacial properties of the anode, ensuring stable contact. These results corroborate earlier findings that the cross-linked binder derived from cis-PBD and BA forms a robust 3D polymer network, which helps maintain intimate interfacial contact within the electrode. Consequently, this well-structured cross-linked binder is demonstrated to be a promising candidate for Si-based composite anodes in ASSLBs, where large volume changes occur during cycling.

## **CONCLUSIONS**

In this work, we fabricated the composite Si-C anodes using a highly adhesive and robust in situ cross-linked binder formed via photoinduced cross-linking of PBD and BA monomer. Among the various isomers of PBD, the 1,4-cis configuration predominantly participated in the cross-linking reaction with BA. The resulting composite Si-C anode incorporating the in situ cross-linked binder derived from cis-PBD and BA exhibited superior cohesive strength and the lowest internal resistance. Consequently, the all-solid-state cell employing this composite Si-C electrode and LPSX electrolyte (Li/LPSX/ Si-C cell) demonstrated superior cycling performance in terms of discharge capacity, cycling stability, and high-rate capability. Furthermore, 2D and 3D morphological analyses of the cycled composite Si-C electrodes revealed that the crosslinked binder effectively suppressed the large volume changes of the Si-C electrode during repeated cycling. These results indicate that the cross-linked binder based on cis-PBD and BA

is a promising candidate for Si-based anodes in high energy density ASSLBs.

## ASSOCIATED CONTENT

# Supporting Information

The Supporting Information is available free of charge at https://pubs.acs.org/doi/10.1021/acsami.5c14778.

Intensities of H<sub>A</sub>, H<sub>B</sub>, and H<sub>B</sub>/H<sub>A</sub> ratio determined from the <sup>1</sup>H NMR spectra; chemical structures and <sup>1</sup>H NMR spectra of n-butyl acrylate, poly(n-butyl acrylate), and cross-linked binders; XRD patterns of LPSX, Si-C, and composite Si-C anodes with different binders; linear sweep voltammograms of LPSX and LPSX/polymer binder composites; voltage profiles of Li/LPSX/Si-C cells during DC-IR tests using different binders; cycling curves of Li/LPSX/Si-C cells with various binders; chemical structures, <sup>1</sup>H and <sup>13</sup>C NMR spectra of PBA and cross-linked binder; HSQC spectra of PBA, BD7BA3-mix, and BD7BA3; cross-sectional SEM and corresponding EDS mapping images of composite Si-C anodes; DC-IR results and resistance for cells with PBD, BD7BA3, and cis-BD7BA3 binders; cycling curves of Li/ LPSX/Si-C cells using PBD and BD7BA3 at various current rates; voltage profiles and pressure changes of the cell; cycling performance of Li/LPSX/Si-C cells with different binders under different stack pressures and charging protocols; X-ray tomographic 2D images of Si-C anodes with PBD, BD7BA3, and cis-BD7BA3 after 200 cycles; and void volume and count in composite Si-C anodes with different binders obtained by XRM analysis (PDF)

# AUTHOR INFORMATION

## **Corresponding Author**

Dong-Won Kim - Department of Chemical Engineering and Department of Battery Engineering, Hanyang University, Seoul 04763, Korea; orcid.org/0000-0002-1735-0272; Phone: +82 2 2220 2337; Email: dongwonkim@ hanyang.ac.kr; Fax: +82 2 2298 4101

#### **Authors**

Young-Jun Lee - Department of Chemical Engineering, Hanyang University, Seoul 04763, Korea

Won-Jae Song - Department of Chemical Engineering, Hanyang University, Seoul 04763, Korea

Yong-Han Jo - Department of Battery Engineering, Hanyang University, Seoul 04763, Korea

Han-Jo Lee - Department of Chemical Engineering, Hanyang University, Seoul 04763, Korea; Advanced Battery Development Team, Hyundai Motor Company, Gyeonggi-do 16082, Korea

Yunsung Kim - Advanced Battery Development Team, Hyundai Motor Company, Gyeonggi-do 16082, Korea Gahyeon Im - Advanced Battery Development Team, Hyundai Motor Company, Gyeonggi-do 16082, Korea

Complete contact information is available at: https://pubs.acs.org/10.1021/acsami.5c14778

## Notes

The authors declare no competing financial interest.

## ACKNOWLEDGMENTS

This work was supported by the Hyundai Motor Company and the National Research Foundation of Korea funded by the Korean government (RS-2024-00454354).

## REFERENCES

- (1) Cano, Z. P.; Banham, D.; Ye, S.; Hintennach, A.; Lu, J.; Fowler, M.; Chen, Z. Batteries and fuel cells for emerging electric vehicle markets. Nat. Energy 2018, 3, 279-289.
- (2) Manzetti, S.; Mariasiu, F. Electric vehicle battery technologies: From present state to future systems. Renew. Sustain. Energy Rev. **2015**, *51*, 1004–1012.
- (3) Famprikis, T.; Canepa, P.; Dawson, J. A.; Islam, M. S.; Masquelier, C. Fundamentals of inorganic solid-state electrolytes for batteries. Nat. Mater. 2019, 18, 1278-1291.
- (4) Cheng, X.-B.; Zhao, C.-Z.; Yao, Y.-X.; Liu, H.; Zhang, Q. Recent Advances in Energy Chemistry between Solid-State Electrolyte and Safe Lithium-Metal Anodes. Chem. 2019, 5, 74-96.
- (5) Wang, C.; Kim, J. T.; Wang, C.; Sun, X. Progress and Prospects of Inorganic Solid-State Electrolyte-Based All-Solid-State Pouch Cells. Adv. Mater. 2023, 35, No. 2209074.
- (6) Jiang, W.; Yan, L.; Zeng, X.; Meng, X.; Huang, R.; Zhu, X.; Ling, M.; Liang, C. Adhesive Sulfide Solid Electrolyte Interface for Lithium Metal Batteries. ACS Appl. Mater. Interfaces 2020, 12, 54876-54883.
- (7) Gao, Z.; Sun, H.; Fu, L.; Ye, F.; Zhang, Y.; Luo, W.; Huang, Y. Promises, Challenges, and Recent Progress of Inorganic Solid-State Electrolytes for All-Solid-State Lithium Batteries. Adv. Mater. 2018, 30, No. 1705702.
- (8) Tian, Y.; Zeng, G.; Rutt, A.; Shi, T.; Kim, H.; Wang, J.; Koettgen, J.; Sun, Y.; Ouyang, B.; Chen, T.; Lun, Z.; Rong, Z.; Persson, K.; Ceder, G. Promises and Challenges of Next-Generation "Beyond Liion" Batteries for Electric Vehicles and Grid Decarbonization. Chem. Rev. 2021, 121, 1623-1669.
- (9) Randau, S.; Weber, D. A.; Kotz, O.; Koerver, R.; Braun, P.; Wever, A.; Ivers-Tiffee, E.; Adermann, T.; Kulisch, J.; Zeier, W. G.; Richter, F. H.; Janek, J. Benchmarking the performance of all-solidstate lithium batteries. Nat. Energy 2020, 5, 259-270.
- (10) Banerjee, A.; Wang, X.; Fang, C.; Wu, E. A.; Meng, Y. S. Interfaces and Interphases in All-Solid-State Batteries with Inorganic Solid Electrolytes. Chem. Rev. 2020, 120, 6878-6933.
- (11) Park, Y.-E.; Oh, M.-K.; Sim, H.-T.; Kim, H.-J.; Cho, Y.-S.; Park, S.-J.; Kim, D.-W. Rationally Designed Li-Ag Alloy with In-Situ-Formed Solid Electrolyte Interphase for All-Solid-State Lithium Batteries. ACS Appl. Mater. Interfaces 2024, 16, 39460-39469.
- (12) Park, K. H.; Bai, Q.; Kim, D. H.; Oh, D. Y.; Zhu, Y.; Mo, Y.; Jung, Y. S. Design Strategies, Practical Considerations, and New Solution Processes of Sulfide Solid Electrolytes for All-Solid-State Batteries. Adv. Energy Mater. 2018, 8, No. 1800035.
- (13) Sakuda, A.; Hayashi, A.; Tatsumisago, M. Sulfide Solid Electrolyte with Favorable Mechanical Property for All-Solid-State Lithium Battery. Sci. Rep. 2013, 3, 2261.
- (14) Casimir, A.; Zhang, H.; Ogoke, O.; Amine, J. C.; Lu, J.; Wu, G. Silicon-based anodes for lithium-ion batteries: Effectiveness of materials synthesis and electrode preparation. Nano Energy 2016, 27, 359-376.
- (15) Tan, D. H. S.; Chen, Y.-T.; Yang, H.; Bao, W.; Sreenarayanan, B.; Doux, J.-M.; Li, W.; Lu, B.; Ham, S.-Y.; Sayahpour, B.; Scharf, J.; Wu, E. A.; Deysher, G.; Han, H. E.; Hah, H. J.; Jeong, H.; Lee, J. B.; Chen, Z.; Meng, Y. S. Carbon-free high-loading silicon anodes enabled by sulfide solid electrolytes. Science 2021, 373, 6562.
- (16) Oh, P.; Yun, J.; Choi, J. H.; Saqib, K. S.; Embleton, T. J.; Park, S.; Lee, C.; Ali, J.; Ko, K.; Cho, J. Development of High-Energy Anodes for All-Solid-State Lithium Batteries Based on Sulfide Electrolytes. Angew. Chem., Int, Ed 2022, 61, No. 202201249.
- (17) Liu, Z.-K.; Deng, S.-S.; Zhou, Y.; Tong, Z.; Liu, J.-K.; Wang, Z.; Guo, M.-J.; Deng, L.; Zhen, Y.; Li, J.-T.; Xu, J.-M.; Sun, S.-G. On-Site Cross-Linking of Polyacrylamide to Efficiently Bind the Silicon Anode

- of Lithium-Ion Batteries. ACS Appl. Mater. Interfaces 2023, 15, 24416–24426.
- (18) Yeom, S. J.; Wi, T.-U.; Ko, S.; Park, C.; Bayramova, B.; Jin, S.; Lee, S. W.; Lee, H.-W. Nitrogen Plasma-Assisted Functionalization of Silicon/Graphite Anodes to Enable Fast Kinetics. *ACS Appl. Mater. Interfaces* **2022**, *14*, 5237–5246.
- (19) Yamamoto, M.; Terauchi, Y.; Sakuda, A.; Kato, A.; Takahashi, M. An amorphous Si film anode for all-solid-state lithium batteries. *J. Power Sources* **2020**, 473, No. 228595.
- (20) Piper, D. M.; Yersak, T. A.; Lee, S.-H. Effect of Compressive Stress on Electrochemical Performance of Silicon Anodes. *J. Electrochem. Soc.* **2013**, *160*, A77.
- (21) Oh, J.; Chung, W. J.; Jung, S. H.; Kim, Y.; Lee, Y.; Nam, Y. J.; Lee, S.; Kim, C. H.; Choi, J. W. Critical impact of volume changes in sulfide-based all-solid-state batteries operating under practical conditions. *Energy Storage Mater.* **2024**, *71*, No. 103606.
- (22) Chae, S.; Choi, S.-H.; Kim, N.; Sung, J.; Cho, J. Integration of Graphite and Silicon Anodes for the Commercialization of High-Energy Lithium-Ion Batteries. *Angew. Chem., Int, Ed* **2020**, *59*, 110–135.
- (23) Li, X.; Yan, P.; Xiao, X.; Woo, J. H.; Wang, C.; Liu, J.; Zhang, J.-G. Design of porous Si/C-graphite electrodes with long cycle stability and controlled swelling. *Energy Environ. Sci.* **2017**, *10*, 1427–1434.
- (24) Lee, K.; Lee, J.; Choi, S.; Char, K.; Choi, J. W. Thiol-Ene Click Reaction for Fine Polarity Tuning of Polymeric Binders in Solution-Processed All-Solid-State Batteries. *ACS Energy Lett.* **2019**, *4*, 94–101.
- (25) Lee, J.; Lee, K.; Lee, T.; Kim, H.; Kim, K.; Cho, W.; Coskun, A.; Char, K.; Choi, J. W. In Situ Deprotection of Polymeric Binders for Solution-Processible Sulfide-Based All-Solid-State Batteries. *Adv. Mater.* **2020**, 32, No. 2001702.
- (26) Hong, S.-B.; Jang, Y.-R.; Kim, H.; Jung, Y.-C.; Shin, G.; Hah, H. J.; Cho, W.; Sun, Y.-K.; Kim, D.-W. Wet-Processable Binder in Composite Cathode for High Energy Density All-Solid-State Lithium Batteries. *Adv. Energy Mater.* **2024**, *14*, 2400802.
- (27) Lee, Y.-J.; Hong, S.-B.; Kim, D.-W. Exploring the use of butadiene rubbers as a binder in composite cathodes for all-solid-state lithium batteries. *J. Ind. Eng. Chem.* **2023**, 122, 341–348.
- (28) Nikodimos, Y.; Huang, C.-J.; Taklu, B. W.; Su, W.-N.; Hwang, B. J. Chemical stability of sulfide solid-state electrolytes: stability toward humid air and compatibility with solvents and binders. *Energy Environ. Sci.* **2022**, *15*, 991–1033.
- (29) Lee, K.; Kim, S.; Park, J.; Park, S. H.; Coskun, A.; Jung, D. S.; Cho, W.; Choi, J. W. Selection of Binder and Solvent for Solution-Processed All-Solid-State Battery. *J. Electrochem. Soc.* **2017**, *164*, A2075.
- (30) Ruhl, J.; Riegger, L. M.; Ghidiu, M.; Zeier, W. G. Impact of Solvent Treatment of the Superionic Argyrodite Li<sub>6</sub>PS<sub>5</sub>Cl on Solid-State Battery Performance. *Adv. Energy Sustainability Res.* **2021**, *2*, No. 2000077.
- (31) Hatz, A.-K.; Calaminus, R.; Feijoo, J.; Treber, F.; Blahusch, J.; Lenz, T.; Reichel, M.; Karaghiosoff, K.; Vargas-Barbosa, N. M.; Lotsch, B. V. Chemical Stability and Ionic Conductivity of LGPS-Type Solid Electrolyte Tetra-Li<sub>7</sub>SiPS<sub>8</sub> after Solvent Treatment. *ACS Appl. Energy. Mater.* **2021**, *4*, 9932–9943.
- (32) Lee, Y.-J.; Hong, S.-B.; Lee, H.-J.; Sim, H.-T.; Kim, Y.; Kim, S.; Kim, D.-W. Flexible and thin sulfide-based solid electrolyte sheet with Li<sup>+</sup>-ion conductive polymer network for all-solid-state lithium-ion batteries. *Chem. Eng. J.* **2023**, *477*, No. 146983.
- (33) Lee, D.; Kondo, A.; Lee, S.; Myeong, S.; Sun, S.; Hwang, I.; Song, T.; Naito, M.; Paik, U. Controlled swelling behavior and stable cycling of silicon/graphite granular composite for high energy density in lithium ion batteries. *J. Power Sources* **2020**, *457*, No. 228021.
- (34) Jo, Y.-H.; Lee, Y.-J.; Kim, D.-W. Exploring the Optimal Binder Content in Composite Electrodes for Sulfide-Based All-Solid-State Lithium-Ion Batteries. *J. Electrochem. Soc.* **2024**, *171*, 100525.
- (35) Leon-Boigues, L.; Perez, L. A.; Mijangos, C. In Situ Synthesis of Poly(butyl methacrylate) in Anodic Aluminum Oxide Nanoreactors by Radical Polymerization: A Comparative Kinetics Analysis by

- Differential Scanning Calorimetry and <sup>1</sup>H-NMR. Polymers 2021, 13, 602.
- (36) Heine, T.; Corminboeuf, C.; Seifert, G. The Magnetic Shielding Function of Molecules and Pi-Electron Delocalization. *Chem. Rev.* **2005**, *105*, 3889–3910.
- (37) Steinmann, S. N.; Jana, D. F.; Wu, J.I.-C.; Schleyer, P. V. R.; Mo, Y.; Corminboeuf, C. Direct Assessment of Electron Delocalization Using NMR Chemical Shifts. *Angew. Chem., Int, Ed* **2009**, *48*, 9828–9833.
- (38) Locke, G.; Bernhard, S. S. R.; Senge, M. O. Nonconjugated Hydrocarbons as Rigid-Linear Motifs: Isosteres for Material Sciences and Bioorganic and Medicinal Chemistry. *Chem.–Eur. J.* **2019**, 25, 4590–4647.
- (39) Hong, S.-B.; Lee, Y.-J.; Kim, U.-H.; Bak, C.; Lee, Y. M.; Cho, W.; Hah, H. J.; Sun, Y.-K.; Kim, D.-W. All-Solid-State Lithium Batteries: Li<sup>+</sup>-Conducting Ionomer Binder for Dry-Processed Composite Cathodes. *ACS Energy Lett.* **2022**, *7*, 1092–1100.
- (40) Edwards, H. G. M.; Johnson, A. F.; O'Brien, M. T.; Dobrowski, S. A. Determination of the relative reactivities of cis and trans isomers of  $\beta$ -bromostyrene towards polystyryllithium by Raman spectroscopy. *J. Mol. Struct.* **2004**, 703, 31–35.
- (41) Dossi, E.; Earnshaw, J.; Ellison, L.; Santos, G. R. D.; Cavaye, H.; Cleaver, D. J. Understanding and controlling the glass transition of HTPB oligomers. *Polym. Chem.* **2021**, *12*, 2606–2617.
- (42) Marzocca, A. J.; Rodriguez Garraza, A. L.; Mansilla, M. A. Evaluation of the polymer–solvent interaction parameter  $\chi$  for the system cured polybutadiene rubber and toluene. *Polym. Test.* **2010**, 29, 119–126.
- (43) Marzocca, A. J.; Garraza, R.; Sorichetti, P.; Mosca, H. O. Cure kinetics and swelling behavior in polybutadiene rubber. *Polym. Test* **2010**, 29, 477–482.
- (44) Son, B.; Ryou, M.-H.; Choi, J.; Lee, T.; Yu, H. K.; Kim, J. H.; Lee, Y. M. Measurement and Analysis of Adhesion Property of Lithium-Ion Battery Electrodes with SAICAS. *ACS Appl. Mater. Interfaces* **2014**, *6*, 526–531.
- (45) Choi, J.; Bak, C.; Kim, J. Y.; Shin, D. O.; Kang, S. H.; Lee, Y. M.; Lee, Y.-G. Enhancing electrochemo-mechanical properties of graphite-silicon anode in all-solid-state batteries via solvent-induced polar interactions in nitrile binders. *J. Energy Chem.* **2025**, *105*, 514–524.
- (46) Cao, D.; Sun, X.; Li, Y.; Anderson, A.; Lu, W.; Zhu, H. Long-Cycling Sulfide-Based All-Solid-State Batteries Enabled by Electrochemo-Mechanically Stable Electrodes. *Adv. Mater.* **2022**, *34*, No. 2200401.
- (47) Li, H.; Chen, Z.; Kang, Z.; Liu, W.; Chen, Y. High-density crack-resistant Si-C microparticles for lithium ion batteries. *Energy Storage Mater.* **2023**, *56*, 40–49.
- (48) Shearing, P. R.; Brandon, N. P.; Gelb, J.; Bradley, R.; Withers, P. J.; Marquis, A. J.; Cooper, S.; Harris, S. J. Multi Length Scale Microstructural Investigations of a Commercially Available Li-Ion Battery Electrode. *J. Electrochem. Soc.* **2012**, *159*, A1023—A1027.
- (49) Oh, J.; Choi, S. H.; Kim, J. Y.; Lee, J.; Lee, T.; Lee, N.; Lee, T.; Sohn, Y.; Chung, W. J.; Bae, K. Y.; Son, S.; Choi, J. W. Anode-Less All-Solid-State Batteries Operating at Room Temperature and Low Pressure. *Adv. Energy Mater.* **2023**, *13*, No. 2301508.